JBMR Plus, 2024, **8**, ziae050
https://doi.org/10.1093/jbmrpl/ziae050
Advance access publication: April 9, 2024
Research Article

Loss-of-function *OGFRL1* variants identified in autosomal recessive cherubism families

Mizuho Kittaka[1,2], Noriyoshi Mizuno[3,*], Hiroyuki Morino[4], Tetsuya Yoshimoto[1,2], Tianli Zhu[2], Sheng Liu[5], Ziyi Wang[6], Kotoe Mayahara[7], Kyohei Iio[8], Kaori Kondo[9], Toshio Kondo[6], Tatsuhide Hayashi[10], Sarah Coghlan[1,2], Yayoi Teno[1,2], Andrew Anh Phung Doan[1,2], Marcus Levitan[1,2], Roy B. Choi[11], Shinji Matsuda[3], Kazuhisa Ouhara[3], Jun Wan[5], Annelise M. Cassidy[12], Stephane Pelletier[12], Sheela Nampoothiri[13], Andoni J. Urtizberea[14], Alexander G. Robling[11], Mitsuaki Ono[6], Hideshi Kawakami[15], Ernst J. Reichenberger[16], Yasuyoshi Ueki[1,2,*]

[1]Indiana Center for Musculoskeletal Health, Indiana University School of Medicine, Indianapolis, IN 46202, United States
[2]Department of Biomedical Sciences and Comprehensive Care, Indiana University School of Dentistry, Indianapolis, IN 46202, United States
[3]Department of Periodontal Medicine, Graduate School of Biomedical and Health Sciences, Hiroshima University, Hiroshima 734-8553, Japan
[4]Department of Medical Genetics, Tokushima University Graduate School of Biomedical Sciences, Tokushima 770-8503, Japan
[5]Indiana University Simon Comprehensive Cancer Center, Indiana University School of Medicine, Indianapolis, IN 46202, United States
[6]Department of Molecular Biology and Biochemistry, Okayama University Medical School, Okayama 700-8558, Japan
[7]Department of Orthodontics, Nihon University School of Dentistry, Tokyo 101-8310, Japan
[8]Department of Pediatrics, Graduate School of Medicine, Kyoto University, Kyoto 606-8507, Japan
[9]Hematology Division, Tokyo Metropolitan Cancer and Infectious Diseases Center, Komagome Hospital, Tokyo 113-8677, Japan
[10]Department of Dental Materials Science, School of Dentistry, Aichi Gakuin University, Aichi 464-8650, Japan
[11]Department of Anatomy, Cell Biology & Physiology, Indiana University School of Medicine, Indianapolis, IN 46202, United States
[12]Department of Medical and Molecular Genetics, Indiana University School of Medicine, Indianapolis, IN 46202, United States
[13]Department of Pediatric Genetics, Amrita Institute of Medical Sciences & Research Centre, Kerala 682041, India
[14]Institut de Myologie, Paris 75013, France
[15]Department of Molecular Epidemiology, Research Institute for Radiation Biology and Medicine, Hiroshima University, Hiroshima 734-8553, Japan
[16]Department of Reconstructive Sciences, School of Dental Medicine, University of Connecticut Health, CT 06030, United States
*Corresponding authors: Noriyoshi Mizuno, Department of Periodontal Medicine, Graduate School of Biomedical and Health Sciences, Hiroshima University, 1-2-3 Kasumi, Minami-Ku, Hiroshima 734-8553, Japan (mizuno@hiroshima-u.ac.jp) and Yasuyoshi Ueki, Department of Biomedical Sciences and Comprehensive Care, Indiana University School of Dentistry, Indiana Center for Musculoskeletal Health, Indiana University School of Medicine, Van Nuys Medical Science Bldg, Rm#514, 635 Barnhill Dr, Indianapolis, IN 46202, United States (uekiy@iu.edu).

Abstract

Cherubism (OMIM 118400) is a rare craniofacial disorder in children characterized by destructive jawbone expansion due to the growth of inflammatory fibrous lesions. Our previous studies have shown that gain-of-function mutations in SH3 domain-binding protein 2 (SH3BP2) are responsible for cherubism and that a knock-in mouse model for cherubism recapitulates the features of cherubism, such as increased osteoclast formation and jawbone destruction. To date, *SH3BP2* is the only gene identified to be responsible for cherubism. Since not all patients clinically diagnosed with cherubism had mutations in SH3BP2, we hypothesized that there may be novel cherubism genes and that these genes may play a role in jawbone homeostasis. Here, using whole exome sequencing, we identified homozygous loss-of-function variants in the opioid growth factor receptor like 1 (*OGFRL1*) gene in 2 independent autosomal recessive cherubism families from Syria and India. The newly identified pathogenic homozygous variants were not reported in any variant databases, suggesting that *OGFRL1* is a novel gene responsible for cherubism. Single cell analysis of mouse jawbone tissue revealed that *Ogfrl1* is highly expressed in myeloid lineage cells. We generated OGFRL1 knockout mice and mice carrying the Syrian frameshift mutation to understand the *in vivo* role of OGFRL1. However, neither mouse model recapitulated human cherubism or the phenotypes exhibited by SH3BP2 cherubism mice under physiological and periodontitis conditions. Unlike bone marrow-derived M-CSF-dependent macrophages (BMMs) carrying the SH3BP2 cherubism mutation, BMMs lacking OGFRL1 or carrying the Syrian mutation showed no difference in TNF-α mRNA induction by LPS or TNF-α compared to WT BMMs. Osteoclast formation induced by RANKL was also comparable. These results suggest that the loss-of-function effects of OGFRL1 in humans differ from those in mice and highlight the fact that mice are not always an ideal model for studying rare craniofacial bone disorders.

Keywords: rare disease, cherubism, autosomal recessive, whole exome sequencing, OGFRL1, mutation, loss of function, mouse model

Received: November 29, 2023. **Revised:** March 1, 2024. **Accepted:** March 24, 2024

Lay Summary

Cherubism is a rare craniofacial disorder in children that causes destructive expansion of the jawbone. Currently, the only known gene responsible for cherubism is SH3 domain-binding protein 2 (*SH3BP2*). We hypothesized that there may be other genes associated with cherubism. We used whole exome sequencing, a genomic technology that sequences all of the protein-coding regions of genes in the genome, and identified homozygous loss-of-function variants in the *OGFRL1* gene in 2 independent autosomal recessive cherubism families. However, mice that have no functional OGFRL1 protein did not exhibit cherubism-like features. The results indicate that the effects of OGFRL1 loss-of-function in humans are distinct from those in mice. This highlights the fact that mice are not always the best model for studying rare craniofacial bone disorders.

Graphical Abstract

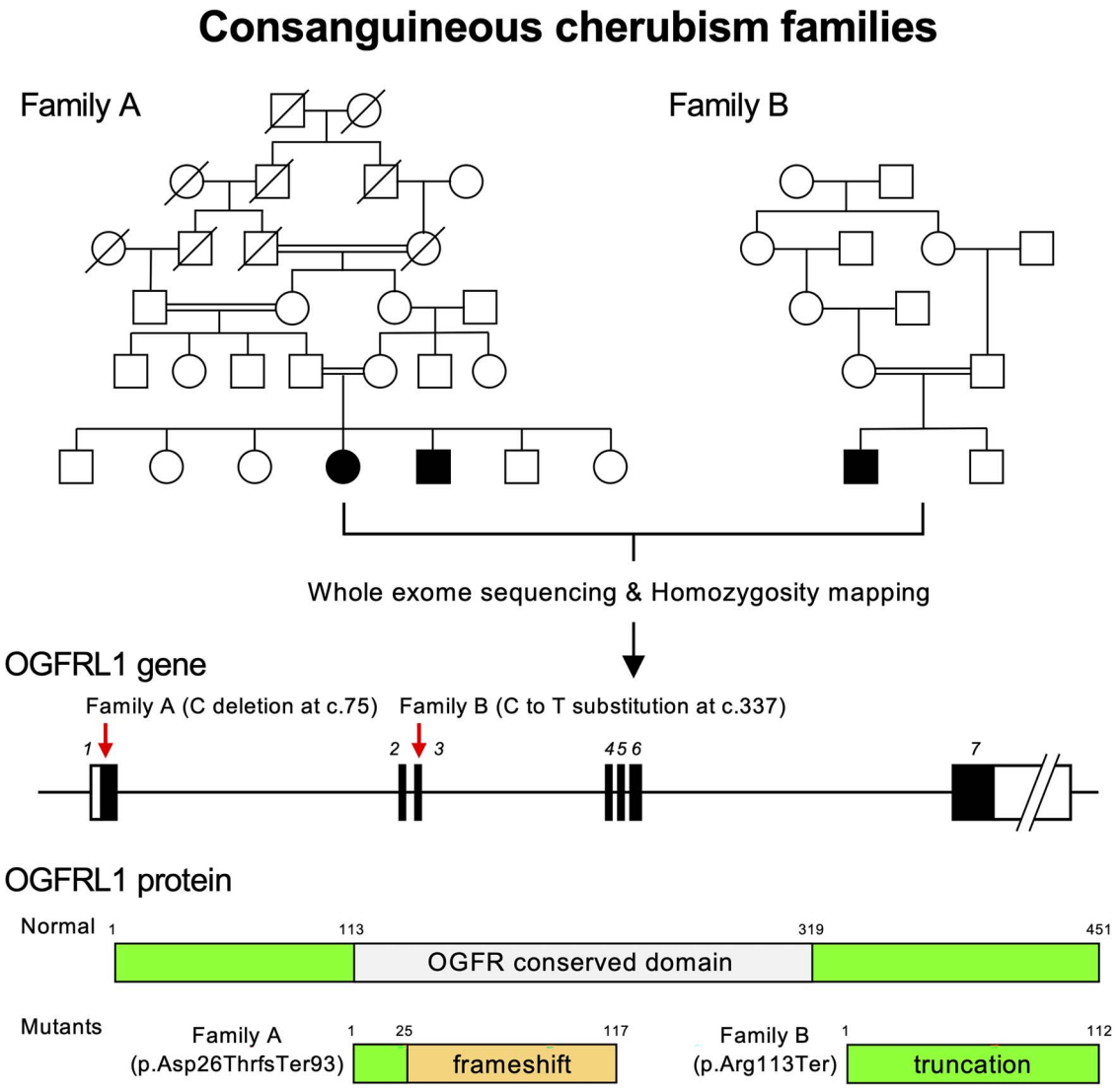

Introduction

Cherubism (OMIM 118400) is a rare jawbone dysplasia in children. It is characterized by bilateral destructive expansion of the mandible due to the growth of fibrous tissue containing large numbers of multinucleated osteoclasts, resulting in the typical cherub angel-like facial swelling.[1,2] The jaw swelling often resolves after puberty by a mechanism that may involve the innate immune response.[3,4] The rapid bone degradation leads to the formation of multiple cysts in the mandible and maxilla. We have previously discovered that heterozygous missense mutations in the tankyrase-binding motif (RSPPDG) of the adaptor protein SH3 domain-binding protein 2 (SH3BP2) are responsible for the most cases of familial and sporadic cherubism.[5,6] The discovery of cherubism mutations in SH3BP2 and the analysis of knock-in mouse models of cherubism revealed critical roles of SH3BP2-regulated signaling pathways in macrophage inflammation, osteoclastogenesis, and the pathogenesis of autoimmune arthritis and periodontitis, beyond its role in cherubism.[3,4,7-15] Thus, cherubism was an excellent example for how the study of rare diseases can provide insights into the mechanism of common diseases. We have previously identified individuals with cherubism-like jawbone dysplasia but no mutations in SH3BP2 in 2 consanguineous families from Syria and India. The objective of this study was to identify a second gene responsible for cherubism by examining

the 2 families and to determine the function of the gene in jaw homeostasis.

Here, we show that whole exome sequencing (WES) combined with homozygosity mapping identified previously unknown homozygous loss-of-function mutations in the gene encoding opioid growth factor receptor like 1 (OGFRL1). OGFRL1 has homology with the opioid growth factor receptor (OGFR) and is a potential orphan receptor with signaling receptor activity and largely unknown function. Next, we investigated whether OGFRL1 deficiency recapitulates cherubism-like phenotypes in mice by creating OGFRL1 knockout mice. However, these mice failed to exhibit the facial swelling, jawbone erosion, jawbone loss, and development of macrophage-rich inflammatory infiltrates, all of which are characteristics of homozygous SH3BP2-mutant cherubism mice. CRISPR/Cas9 knock-in mice carrying the homozygous mutation equivalent to that found in the Syrian family also failed to exhibit these phenotypes. These results suggest that OGFRL1 plays a specific role in the development of fibrous dysplasia of the jawbone in humans, but a weaker role in mice. Identification of further OGFRL1 mutations in cherubism patients and clinical characterization of the patients will be important to determine the function of OGFRL1 in craniofacial development and integrity and oral immune responses.

Materials and methods

Cherubism families

Family members were recruited according to the protocols approved by the Institutional Review Board of University of Connecticut Health. Informed consent was obtained from all study participants by their treating physicians according to the ethics guidelines of their institutions. All genetic and experimental methods were carried out in accordance with relevant guidelines and regulations. Affected individuals underwent thorough clinical diagnosis.

Exome sequencing, homozygosity mapping, and variant filtering

Exome sequencing (NimbleGen SeqCap EZ Exome 64 Mb capture kit, 200X coverage) was performed using genomic DNA isolated from peripheral lymphocytes of affected individuals as previously described.[16] SNP genotyping was performed using the Genome-Wide Human SNP Array 6.0 (Affymetrix). We used homozygosity mapping to obtain the identity by descent with a resolution of 3 centimorgans.[17] Candidate variants were filtered based on open databases (dbSNP build 135, the 1000 Genomes Project), genomic positions, and zygosities. Variants observed in the in-house database were also excluded. Exonic variants localized in homozygosity regions were selected as candidates for cherubism mutations, and the pathogenicity of exonic variants was evaluated by Franklin or Varsome in combination with PolyPhen-2, Mutation Taster, and SIFT. Candidate variants were confirmed by Sanger sequencing (ABI 3130; Thermo Fisher Scientific).

Mice

All animal experiments were conducted under the animal protocol approved by the IACUC of Indiana University School of Medicine. *Ogfrl1*-floxed ($Ogfrl1^{fl/fl}$) mice were generated by inGenious Targeting Laboratory. The targeting construct harboring *Ogfrl1* exon 2 and 3 flanked by LoxP sites and the neomycin-resistance cassette flanked by flippase recombinase target (FRT) sites was electroporated to hybrid (C57BL/6 × 129/SvEv) embryonic stem (ES) cells (Supplementary Figure S1). Electroporated ES cells were then cultured in medium containing G418 for positive selection. Targeted ES cell clones were identified by PCR and confirmed by the Southern blot, and one of the ES cell clones was used for generating chimera mice. Chimera mice were bred with flippase (FLP) recombinase transgenic mice for *in vivo* excision of the neomycin cassette. Mice carrying the *Ogfrl1*-floxed allele were crossed with *EIIa-Cre* mice to obtain heterozygous OGFRL1-deficient mice ($Ogfrl1^{+/-}$), then backcrossed to C57BL/6 J mice for at least 7 times ($N = 7$). Heterozygous $Ogfrl1^{+/-}$ male and female mice were crossed to produce homozygous OGFRL1-deficient ($Ogfrl1^{-/-}$) and control $Ogfrl1^{+/+}$ mice. $Ogfrl1^{Del\text{-}c/+}$ mice on the C57BL/6JN background that have the OGFRL1 mutation equivalent to that identified in the Syrian family were created at the Indiana University Genome Editing Center by using the CRISPR-Cas9 system, in which the guide RNA (CTCCGAATCGGTCTGCCAGG) and homology-directed repair template (TCAATGGGCAACCTGCTCG-GCGGGGTCAGCTTCCGCGAGCCCACCACCGTGGAG-GACTGCGAC*AGTACT*TGGCAGACGATTCGGAGCCCG AGCCCGAGCAGCCGGGGCCGGCAGGCGGTGGCGAG GGCCAGCAGCACGACGAGCCGGAGCAGCCCAAGCA, underline = silent mutations for ScaI digestion) were used. Heterozygous $Ogfrl1^{Del\text{-}c/+}$ male and female mice backcrossed to C57BL/6 J mice for 2 generations were crossed to obtain homozygous $Ogfrl1^{Del\text{-}c/Del\text{-}c}$ and control $Ogfrl1^{+/+}$ mice. All mice were bred and housed under specific-pathogen-free (SPF) conditions.

MicroCT analysis

Jawbone tissues were fixed with 4% paraformaldehyde for overnight and soaked in 70% ethanol before scanning with the Skyscan 1176 (Bruker). The following conditions were used: 50 kV, 8.43 μm pixel size, 0.3-degree rotation step, and 926-ms exposure time. Scanned data were reconstructed with the NRecon software (Bruker) with the 0 to 0.12 dynamic range for jawbones and 0 to 0.18 dynamic range for calvariae. The datasets were aligned with the DataViewer (Bruker). Volumetric and linear analyses were performed for jawbones. For volumetric analysis, alveolar bone between 2 buccal roots underneath the maxillary second molar, which is composed of 16 slices (approximately 140-μm thickness), was segmented as the ROI, and the bone volume (BV) was measured by CT-Analyzer (Bruker) with a threshold value of 60. Jawbones with tooth root fusion in the second molar were excluded from the analysis.[18] For linear analysis, the total distance between cementoenamel junction and alveolar bone crest (CEJ-ABC distance) underneath the 4 cusps of the second molar was measured. For calvarial bone analysis, a threshold value of 48 was used. Calvarial bone damage was assessed with BS/TV (surface roughness) and BV/TV as we have previously performed.[19]

Ligature-induced periodontitis

The maxillary left second molar of 10-wk-old male and female mice was ligated with 5-0 silk sutures (Ethicon) for 5 days. The maxillary right second molar was left unligated to serve as a control of alveolar bone analysis. Male and female mice were analyzed separately. To calculate the BV reduction rate (bone

loss %) caused by ligature placement, the following formula was used: {(BV of unligated side − BV of ligated side)/BV of unligated side} × 100.

Histology and histomorphometry of tartrate-resistant acid phosphatase-positive osteoclasts

After μCT analysis, jawbone tissues were decalcified with EDTA (0.5 M, pH =7.2) and processed with graded ethanol for dehydration, xylene for clearing, and hot liquid paraffin for infiltration. The tissues were then embedded in paraffin. The paraffin blocks were sectioned at 6 μm thickness. Sagittal sections and coronal sections were collected on positive-charged slides, followed by H&E and tartrate-resistant acid phosphatase (TRAP) staining. For histomorphometric analysis of osteoclasts, the number of osteoclasts, osteoclast surface, and bone surface was measured on TRAP-stained sections of alveolar bone between 2 buccal roots of the maxillary second molar using the ImageJ software (NIH). Results from 2 sections separated by 20 to 50 μm were averaged. Bone samples from unligated mice or the unligated right side were used as controls. Measurements were performed by personnel blinded to sample information.

Dual-energy X-ray absorptiometry

Isoflurane-anesthetized mice were scanned on a PIXImus II densitometer (GE Lunar) at 4, 8, 12, 16, and 24 wk of age. Lean mass, fat mass, bone area, BMC, and areal BMD were measured for the whole body (excluding the skull and tail), LS (L3- L5), and right lower limb (distal to the acetabulum) using the Lunar ROI tools.

Calvarial injection with LPS or TNF-α

Ultra-pure LPS from *Escherichia coli* (0111:B4) (100 μg in 20 μL PBS/injection, Invivogen) was injected twice in an interval of 48 h, then analyzed at 48 h after the last injection. Mouse recombinant TNF-α (1 μg in 20 μL PBS/injection, PeproTech) was injected daily for 5 times, then analyzed at 24 h after the last injection. For vehicle controls, mice received PBS (20 μL/injection).

Bone marrow-derived M-CSF-dependent macrophage culture

BM cells from tibiae and femurs were collected from 7- to 8-wk-old mice. Red blood cell-free BM cells were incubated with α-Minimum Essential Medium (MEM) containing 10% FBS and penicillin/streptomycin for 3 h on Petri dishes. Non-adherent BM cells were seeded onto 6-well plates (5.0×10^5 cells/well) and cultured with M-CSF (25 ng/mL, PeproTech) for 4 days to expand bone marrow-derived M-CSF-dependent macrophages (BMMs). Subsequently, BMMs were cultured without M-CSF for 4 h, then stimulated with *E. coli* LPS (Invivogen) or mouse recombinant TNF-α (PeproTech).

RNA-seq analysis of BMMs

BMMs isolated from tibia and femur of *Ogfrl1*$^{-/-}$ and littermate control *Ogfrl1*$^{+/+}$ mice were lysed to isolate total RNA. RNA-seq analysis was conducted at the Indiana University Center of Medical Genomics. Sequence data were mapped with the RNA-seq aligner STAR. Differentially expressed genes (DEGs) were analyzed using the edgeR software.

Single-cell RNA-seq analysis of jawbone cells and BM cells

Single-cell RNA-seq experiment was conducted at the Indiana University Center of Medical Genomics. Maxillae and mandibles were obtained from 8- to 10-wk-old C57BL/6 J male WT mice. After the removal of incisors and molars, the remaining jawbone tissues were cut in small pieces (approximately 2 × 2 mm in size), then serially digested with type I collagenase (250 U/mL, Worthington Biochemical) in α-MEM and EDTA (5 mM, pH = 7.4, ACROS Organics) in Ca- and Mg-free Hanks' Balanced Salt Solution (HBSS) as previously described.[19] Each digestion step was performed for 30 min under 170 rpm shaking in a CO_2 incubator (5% at 37°C). Cells obtained from the second to the ninth digestion steps were pooled and cultured on dishes coated with type I collagen for 48 ho. Non-adherent cells were removed and remaining adherent cells were used as jawbone cells.

BM cells were flushed out from tibiae and femurs of 10-wk-old *Ogfrl1*$^{-/-}$ and *Ogfrl1*$^{+/+}$ mice using HBSS, then treated with RBC lysis buffer (Invitrogen) for 4 min to remove red blood cells. Cell suspensions were further treated with histopaque 1083 (Sigma-Aldrich) to minimize the contamination with dead cells. About 20 000 cells were loaded on a multiple-channel micro-fluidics chip of the Chromium Single Cell Instrument (10X Genomics) with a targeted cell recovery of 10 000. Single cell gel beads in emulsion containing barcoded oligonucleotides and reverse transcriptase reagents were generated with the v3.1 Next GEM Single Cell 3′ reagent kit (10X Genomics). Following cell capture and cell lysis, cDNA was synthesized and amplified. An Illumina sequencing library was then prepared with the amplified cDNA. The resulting library was sequenced on the Illumina NovaSeq 6000. 150 bp including cell barcode and unique molecular identifier (UMI) sequences and 100 bp RNA reads were sequenced. Cell Ranger 5.0.1 (10X Genomics) was utilized to process the raw sequence data. Briefly, cellranger mkfastq was implemented to demultiplex raw base sequence calls generated from the Illumina sequencer into sample-specific FASTQ files. The FASTQ files were then aligned to the mouse reference genome mm10 with the STAR aligner. The aligned reads were traced back to individual cells and the gene expression level of individual genes was quantified based on the number of UMIs detected in each cell. The filtered feature-cell barcode matrices generated by CellRanger were used for further analysis. The R package SoupX version 1.5.2 was used to remove the ambient RNA from the data. The R package Seurat version 4.0 was used for analyses.

Osteoclast differentiation assay

Non-adherent BM cells were cultured on Petri dishes with M-CSF (25 ng/mL) for 3 days for differentiation into BMMs. BMMs were harvested and cultured on 48-well plates (2.5×10^4 cells/well) and further stimulated with M-CSF (25 ng/mL) and RANKL (50 ng/mL; PeproTech) for 3 days. Osteoclasts were visualized with TRAP staining. TRAP-positive cells with more than 3 nuclei were counted by the OC_Finder.[20]

Osteoclast resorption assay

BMMs were seeded on Osteo assay plates (Corning) at a density of 8.3×10^3 cells/well, and further stimulated with M-CSF (25 ng/mL) and RANKL (50 ng/mL) for 7 days. After

removing cells with 10% bleach, non-resorbed areas were identified by von Kossa staining. Resorbed area (%) per well was measured by the ImageJ software (NIH).

Serum TNF-α

Serum TNF-α levels were measured by Mouse TNF-α DuoSet ELISA kit (R&D Systems). Sera were separated from blood using vacutainer collection tubes (BD) and stored at –80°C until use.

qPCR analysis

cDNAs were synthesized from 500 ng of total RNA using a High-Capacity cDNA Reverse Transcription Kit (Applied Biosystems). PowerUP SYBR Green Master Mix (Applied Biosystems) was used for the qPCR reaction in the QuantStudio 3 (Applied Biosystems). Gene expression levels were calculated using the relative standard curve method. *Gapdh* was used as an internal control for normalizing target gene expression. Primer sequences are listed in figure legends of Supplementary Figures.

Statistical analysis

Student's *t*-test or one-way ANOVA followed by Tukey–Kramer post hoc test were used to compare groups. $P < .05$ was considered as statistically significant. Males and females were analyzed separately.

Results

Identification of homozygous loss-of-function OGFRL1 mutations in autosomal recessive cherubism families

We have previously reported that there are patients diagnosed with cherubism who do not have mutations in SH3BP2, suggesting that a second gene responsible for cherubism may exist.[5] We had identified a consanguineous family affected with fibrous dysplasia of the jaw diagnosed with cherubism without mutations in SH3BP2 from Syria. WES with 200 X coverage was performed using DNA samples isolated from 2 affected individuals in the family (Figure 1A, #6 and 7 in the pedigree). We worked with the hypothesis that cherubism in this consanguineous family is inherited as an autosomal recessive trait and that homozygous mutations located within the identical-by-descent regions of the genome are responsible for cherubism in this family. We searched for homozygous DNA variants shared by the 2 affected individuals and identified 6 exonic DNA variants on autosomal chromosomes (Supplementary Table S1A). To genetically exclude genes that are not linked to cherubism, we chose a homozygosity mapping approach and identified 4 homozygous genomic regions that are common in the 2 affected individuals using human genome assembly GRCh37 between: (1) rs838730 and rs4853963 on chromosome 2, (2) rs9453014 and rs16873343 on chromosome 6, (3) rs1957923 and rs12880358 on chromosome 14, and (4) rs6085399 and rs4815533 on chromosome 20 (Supplementary Table S1B). Three homozygous variants in the *COL6A3* (coding collagen type VI alpha 3 chain on chromosome 2), *OGFRL1* (coding OGFRL1 on chromosome 6), and *SETD3* (coding SET domain containing 3, actin N3(tau)-histidine methyltransferase on chromosome 14) were located within these homozygous regions. Strikingly, only the *OGFRL1* variant, which deletes a cytosine in exon 1 of the gene (NM_024576.5:c.75del, hereafter referred as c.75delC), was apparently pathogenic and definitely disrupted the OGFRL1 protein structure due to a frameshift (NP_078852.3:p.(Asp26ThrfsTer93)), resulting in the lack of the OGFR conserved domain (pfam04664, Figure 1B). Furthermore, the *OGFRL1* variant was the only novel variant that is not reported in the Genome Aggregation Database (gnomAD v4.0.0, https://gnomad.broadinstitute.org). Sanger sequencing confirmed the c.75delC homozygous mutation only in affected individuals, but not in unaffected members of the family (Figure 1A and C). We also searched for common compound heterozygous variants in the 2 affected individuals and found that *DTX3*, *KMT2B*, and *SCAF1* variants are likely to be pathogenic (Supplementary Table S1C).

Next, WES analysis was performed on an affected individual in another consanguineous cherubism family from India (Figure 1D). We looked for homozygous and compound heterozygous gene variants that are predicted to be likely pathogenic and carefully examined whether these variants exist within the cherubism candidate genes identified in the Syrian family (Supplementary Table S1D and E). Notably, we identified *OGFRL1* as the only gene that overlapped between the candidate genes from the 2 cherubism families. The homozygous cytosine-to-thymine substitution (NM_024576.5:c.337C > T, hereafter referred as c.337C > T) in exon 3 of the *OGFRL1* resulted in the generation of a premature stop codon (NP_078852.3:p.(Arg113Ter)) (Figure 1E). The affected individual in the Indian family did not have homozygous variants in either *COL6A3* or *SETD3*, nor did he have compound heterozygous variants in either *DTX3*, *KMT2B*, or *SCAF1*. Sanger sequencing confirmed the c.337C > T homozygous mutation in the affected individual (Figure 1F). Interestingly, the c.337C > T putative loss-of-function allelic variant was counted 24 times in 1 612 002 allele numbers in the gnomAD v4.0.0 dataset (rs140294148; 21 counts from non-Finnish European, 1 count from African/African American, 1 count from South Asian, and 1 count from remaining populations). However, no homozygous individuals were reported in these populations (https://gnomad.broadinstitute.org/variant/6-71293548-C-T?dataset=gnomad_r4). Taken together, our WES analysis identified loss-of-function mutations in *OGFRL1* for 2 genetically distinct families affected with autosomal recessive cherubism, strongly suggesting that *OGFRL1* is a novel gene responsible for cherubism.

Mice lacking OGFRL1 or carrying the mutation equivalent to that in the Syrian family do not recapitulate jaw dysplasia

We have previously demonstrated that homozygous SH3BP2 knock-in (P416R) cherubism mice ($Sh3bp2^{KI/KI}$) recapitulate the major characteristics of cherubism, such as facial swelling with closed eyelids, jawbone destruction, alveolar bone loss, and increased osteoclastogenesis under SPF and even germ-free conditions.[3,7] To generate a new mouse model for cherubism and investigate the role of OGFRL1 *in vivo*, we created OGFRL1 knockout mice ($Ogfrl1^{-/-}$) by deleting exon 2 and 3 of the *Ogfrl1* gene (Supplementary Figure S1). The homology of the consensus coding sequence between human *OGFRL1* (34482.1) and mouse *Ogfrl1* (35526.1) is approximately 82.0%. Likewise, OGFRL1 protein identity (human Q5TC84 vs mouse Q8VE52) is approximately 79.1%, indicating a functional similarity of OGFRL1 between humans and mice. The $Ogfrl1^{-/-}$ mice were fertile and grew normally until

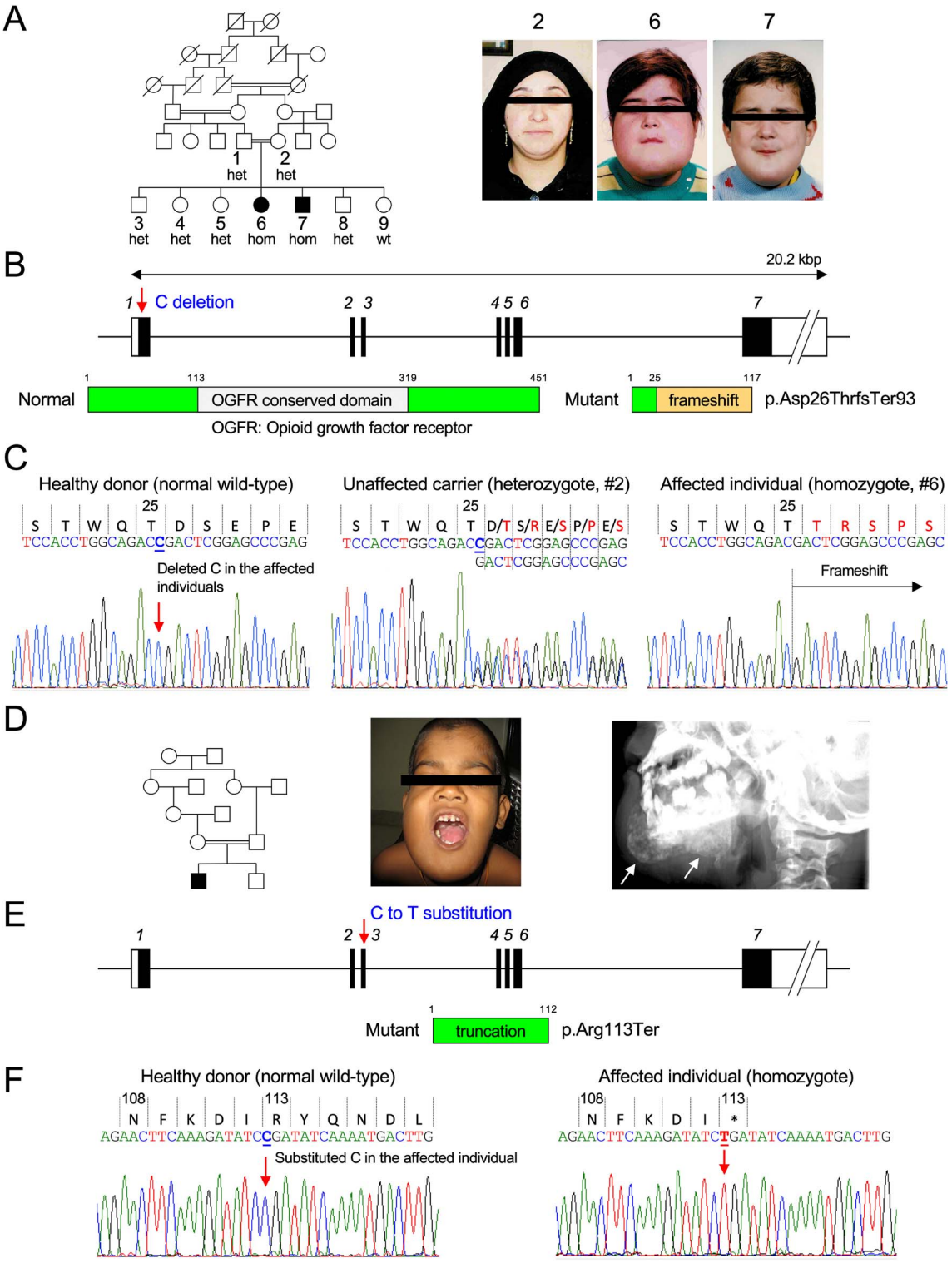

Figure 1. Loss-of-function mutations in the *OGFRL1* gene identified in families affected with an autosomal recessive form of jawbone dysplasia; (A) left: the pedigree of a Syrian family affected with autosomal recessive jawbone dysplasia diagnosed with cherubism; right: facial appearances of individuals #2, 6, and 7; (B) top: the gene structure of *OGFRL1*; a red arrow indicates the location of the homozygous NM_024576.5:c.75del mutation (hereafter referred as c.75delC); bottom left: location of the putative OGFR conserved domain in OGFRL1; bottom right: frameshifted OGFRL1 protein (NP_078852.3:p.(Asp26ThrfsTer93)) due to the c.75delC mutation; (C) electropherograms of partial sequences of exon 1 of *OGFRL1* showing the normal wt sequence and the heterozygous (het) or homozygous (hom) c.75delC mutation; Sanger sequencing confirmed that #1, 2, 3, 4, 5, 8 are heterozygous for the mutation, #6 and 7 are homozygous for the mutation, #9 has the WT sequence; (D) left: the pedigree of an Indian family affected with autosomal recessive jawbone dysplasia diagnosed as cherubism; middle: facial appearance of an affected individual; right: an X-ray image of the jawbone of the affected individual; white arrows indicate the expansile mandible; (E) top: the location of the homozygous NM_024576.5:c.337C > T mutation (hereafter referred as c.337C > T) in *OGFRL1* found in the Indian family (red arrow); this gene mutation generated a truncated OGFRL1 protein (NP_078852.3:p.(Arg113Ter), hereafter referred as p.Arg113Ter) lacking the OGFR conserved domain; bottom: truncated OGFRL1 protein due to p.Arg113Ter mutation; (F) electropherograms of partial sequences of exon 3 of *OGFRL1* showing the WT sequence and the homozygous c.337C > T mutation; (A, D) filled box = affected male; filled circle = affected female; open box = unaffected male; open circle = unaffected female; (B, E) filled boxes = exons coding for OGFRL1 protein; open boxes = 5′ and 3′ UTRs.

24 wk of age (Supplementary Figure S2). However, unlike *Sh3bp2*$^{KI/KI}$ mice, *Ogfrl1*$^{-/-}$ mice did not exhibit swollen face, alveolar bone loss, jawbone erosion, inflammatory infiltrates in the gingiva, or inflammatory bone erosion on the calvaria (Figure 2A–F). In contrast to *Sh3bp2*$^{KI/KI}$ mice, there was no increase in serum TNF-α levels in *Ogfrl1*$^{-/-}$ mice (data not shown).

We and others have shown that SH3BP2 cherubism mutations increase macrophage inflammation and osteoclastogenesis.[3,4,7,8,21] Since we found that *Ogfrl1* is highly expressed in monocyte and macrophage populations (Supplementary Figure S3A and B), we hypothesized that the lack of OGFRL1 may promote inflammatory responses of macrophages and osteoclast formation induced by RANKL *in vitro*. Unexpectedly, BMMs from *Ogfrl1*$^{-/-}$ mice showed *Tnf* upregulation induced by LPS or TNF-α at comparable levels to BMMs from *Ogfrl1*$^{+/+}$ mice (Supplementary Figure S3C). There was no difference in the capacity to form TRAP-positive (+) multinucleated cells in the presence of RANKL between *Ogfrl1*$^{+/+}$ and *Ogfrl1*$^{-/-}$ BMMs (Supplementary Figure S3D). The mineral resorption capacity was comparable between *Ogfrl1*$^{+/+}$ and *Ogfrl1*$^{-/-}$ TRAP+ multinucleated cells (Supplementary Figure S3E). *In vivo*, no increase in osteoclast formation was observed on the alveolar BS (Figure 2G). Consistent with these observations, we were not able to identify DEGs between BMMs from *Ogfrl1*$^{+/+}$ and *Ogfrl1*$^{-/-}$ mice (Supplementary Figure S3F). In addition, single-cell RNA-seq analysis of BM cells from *Ogfrl1*$^{-/-}$ mice did not identify cell clusters that were significantly different from *Ogfrl1*$^{+/+}$ mice (Supplementary Figure S4A and B). The gene expression profile of each cluster was almost identical between *Ogfrl1*$^{+/+}$ and *Ogfrl1*$^{-/-}$ BM cells (Supplementary Figure S4C). It is also known that the SH3BP2 cherubism mutation increases the susceptibility to alveolar bone loss caused by periodontitis.[13] We challenged *Ogfrl1*$^{-/-}$ mice with ligature-induced periodontitis and found that loss-of-function of OGFRL1 did not increase the susceptibility to periodontitis (Figure 2H). Next, *Ogfrl1*$^{-/-}$ mice were challenged by calvarial injection with LPS or TNF-α. We found a slight increase in bone erosion by LPS in *Ogfrl1*$^{-/-}$ mice compared to *Ogfrl1*$^{+/+}$ mice only in males, but we did not find a significant difference by TNF-α injection for both sexes (Supplementary Figure S5A and B).

Next, we hypothesized that the frameshifted *OGFRL1* gene product by the c.75delC mutation may have a dominant negative effect to causes cherubism. To test this hypothesis, a cytosine deletion in exon 1 of the *Ogfrl1* gene, equivalent to the mutation discovered in the Syrian family, was introduced in mice using the CRISPR/Cas9 technology (Supplementary Figure S6A–D). However, none of the phenotypes observed in the SH3BP2 cherubism mice were recapitulated in the *Ogfrl1*$^{Del\text{-}c/Del\text{-}c}$ mice or in the *Ogfrl1*$^{Del\text{-}c/Del\text{-}c}$ BMMs (Figure 3A–H, Supplementary Figure S7A and B). Taken together, these data suggest that a simple loss-of-function of OGFRL1 does not lead to a cherubism-like phenotype in mice and that the cherubism-causing mechanism by OGFRL1 mutations may be specific for humans.

Discussion

In 2001, *SH3BP2* was identified as the first gene responsible for cherubism.[5] In this study, approximately 80% of cherubism cases had mutations in SH3BP2. A more recent study also reported a cherubism case with no mutations in SH3BP2.[22] Pathogenetically, all SH3BP2 mutations associated with cherubism were heterozygous missense mutations located in exon 9, which encodes the RSPPDG tankyrase-binding motif.[6,23] These mutations caused the escape of SH3BP2 protein from ubiquitin-mediated proteasome degradation, resulting in the upregulation of downstream signaling involving SYK in macrophages and osteoclasts.[3,6] During the current study, we found that 5 different pathogenic DNA variants in the tankyrase-binding motif that cause cherubism were counted in the gnomAD database (2 counts for R415Q and P418R, one count for P418T, P418L, and P418H. Total 7 counts in about 1 435 000 alleles), suggesting that cherubism is more prevalent than we thought. The creation and analysis of knock-in mouse models for cherubism and SH3BP2-deficient mice revealed that SH3BP2 is a critical regulator of myeloid cell activation, osteoclastogenesis, and the development of periodontitis, inflammatory arthritis, and autoimmune diseases.[3,4,7-15] Thus, findings from the cherubism study exemplify the long-standing notion that the study of rare diseases often provides important insights into normal physiology and contributes to the understanding of mechanisms for more common diseases.

The aim of this study was to discover a novel gene responsible for cherubism and to demonstrate that this gene plays an important role in jawbone integrity and remodeling. To achieve this goal, we investigated 2 consanguineous families with cherubism without mutations in SH3BP2. WES analysis of affected individuals identified novel homozygous loss-of-function mutations in the gene encoding OGFRL1, whose molecular functions and cellular roles are poorly understood. Homozygosity mapping of one of the families supported that OGFRL1 is the novel cherubism gene. OGFRL1 is a member of a family of proteins that share the conserved OGFR domain. OGFRL1 shares 36.1% amino acid homology with OGFR. OGFR is known to be expressed in a variety of tissues and organs and is activated by the opioid peptide growth factor (OGF), which is chemically termed Met^5-enkephalin, in corneal epithelial cells, endothelial cells, and epidermal keratinocytes, as well as in T/B cells.[24-31] The OGF-OGFR axis has been shown to regulate the *in vivo* functions of osteoblasts and osteocytes and to be involved in the *in vitro* differentiation of mesenchymal stem cells into osteoblasts and the proliferation of cancer cells.[32-39] In contrast, *Ogfrl1* is predominantly expressed in the brain, BM, and spleen.[40] In the BM, myeloid lineage cells express higher levels of *Ogfrl1*,[40] which is supported by the single-cell analysis in our current study. At present, the only function known about OGFRL1 is its capacity to promote the hepatic cell regeneration in mice.[40]

First, we explored the *in vivo* significance of OGFRL1 by generating both global OGFRL1-deficient mice and OGFRL1 Syrian knock-in mutant mice. Based on the successful recapitulation of key features of human cherubism in SH3BP2 P416R mice, we expected that these OGFRL1 mutant mice would exhibit facial swelling with abnormal jawbone resorption.[7] Unexpectedly, neither knockout nor knock-in lines showed any signs of cherubism-like facial appearance or jawbone erosion. Since we have previously shown that heterozygous SH3BP2 cherubism mice have increased susceptibility to inflammatory bone resorption induced by periodontitis and calvarial TNF-α injection,[8,13] we challenged OGFRL1 loss-of-function mice with these inflammatory inducers. However,

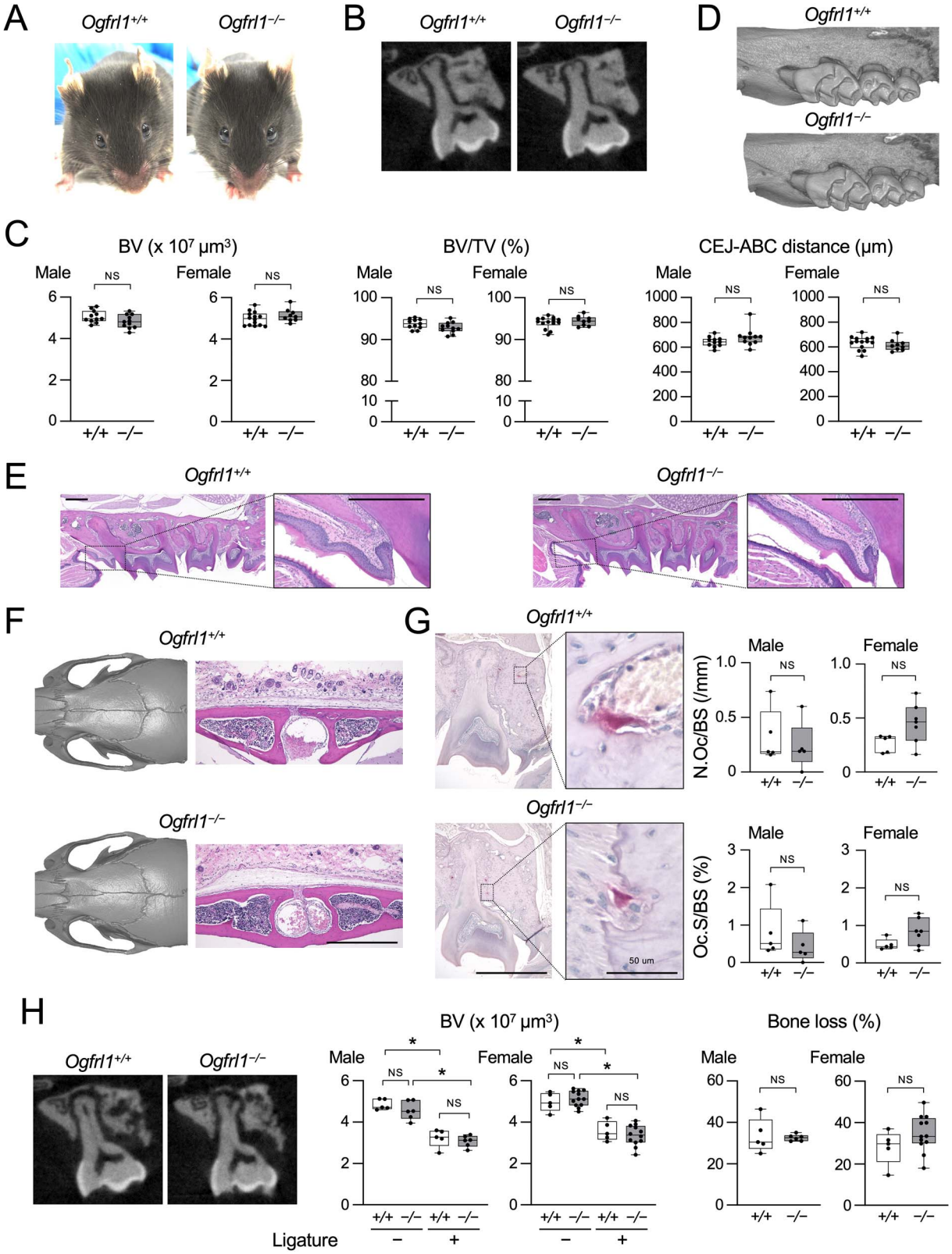

Figure 2. OGFRL1 knockout mice fail to recapitulate human cherubism; (A) facial appearance of OGFRL1-deficient male mice at 12 wk old; (B) two-dimensional microCT images of alveolar bone at the maxillary second molar; (C) microCT analysis of the alveolar bone underneath the maxillary second molar and the CEJ-ABC distance of the maxillary second molar; $n = 11, 11, 14, 9, 11, 11, 14, 9, 11, 11, 14, 9$ from left to right; (D) three-dimensional microCT images of the maxilla and 3 molars; (E) H&E staining images of the maxilla; (F) three-dimensional microCT images of the calvaria and H&E staining images of calvarial tissues; (G) TRAP staining of the alveolar bone underneath the maxillary second molar and histomorphometric analysis for osteoclasts; $n = 5, 5, 5, 7$ from left to right for both N.Oc/BS and Oc.S/BS; (H) left: two-dimensional microCT images of the alveolar bone at the maxillary second molar after ligature placement; right: microCT analysis of BV underneath the maxillary second molar with or without ligature placement and the percentage of alveolar bone loss underneath the maxillary second molar after ligature placement; $n = 5, 6, 5, 6, 5, 12, 5, 12, 5, 6, 5, 12$ from left to right; (E, F, G) bar = 500 μm. $*P < .05$ with Tukey–Kramer post hoc test; NS = not significant; data are presented with box and whisker plots.

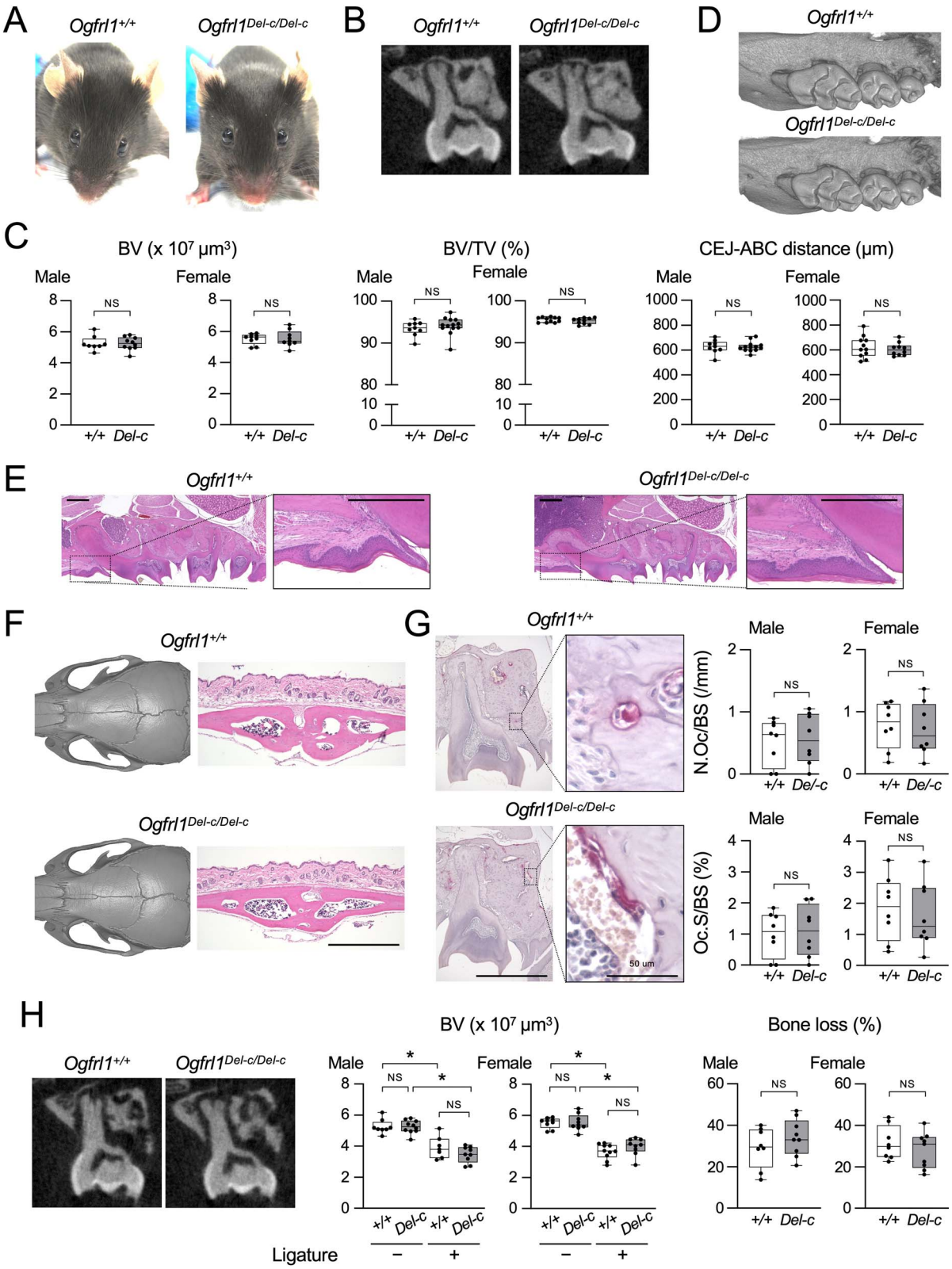

Figure 3. OGFRL1 mice carrying a mutation equivalent to that in the Syrian family fail to recapitulate human cherubism; (A) facial appearance of OGFRL1 knock-in male mice at 12 wk old; (B) two-dimensional microCT images of alveolar bone at the maxillary second molar; (C) microCT analysis of the alveolar bone underneath the maxillary second molar and the CEJ-ABC distance of the maxillary second molar; $n = 8, 10, 9, 9, 9, 13, 11, 10, 9, 13, 11, 10$ from left to right; (D) three-dimensional microCT images of the maxilla and three molars; (E) H&E staining images of the maxilla; (F) three-dimensional microCT images of the calvaria and H&E staining images of calvarial tissues; (G) TRAP staining of the alveolar bone underneath the maxillary second molar and histomorphometric analysis for osteoclasts; $n = 8, 8, 8, 8$ from left to right for both N.Oc/BS and Oc.S/BS; (H) left: two-dimensional microCT images of the alveolar bone at the maxillary second molar after ligature placement; right: microCT analysis of BV underneath the maxillary second molar with or without ligature placement and the percentage of alveolar bone loss underneath the maxillary second molar after ligature placement; $n = 8, 10, 7, 9, 9, 9, 10, 9, 8, 9, 8, 9$ from left to right; (C, G, H) *Del-c* = *Del-c/Del-c* homozygote. (E, F, G) bar = 500 μm. $*P < .05$ with Tukey–Kramer post hoc test; NS = not significant; data are presented with box and whisker plots.

no significant increase in bone loss was observed. These data suggest that the loss-of-function effects of OGFRL1 in humans may be much greater and more impactful than in mice and that the pathogenesis of cherubism caused by loss-of-function mutations of OGFRL1 is fundamentally different from that caused by gain-of-function mutations of SH3BP2. To investigate whether OGFRL1 has any genetic interactions with SH3BP2, we further generated *Sh3bp2*$^{KI/+}$ mice on the *Ogfrl1*$^{-/-}$ background (*Ogfrl1*$^{-/-}$;*Sh3bp2*$^{KI/+}$). However, these compound mutants did not develop facial swelling or jawbone erosion (data not shown), suggesting that OGFRL1 and SH3BP2 act independently to cause human cherubism.

In agreement with observations suggesting differences in the effect of OGFRL1 between humans and mice, similar differences have been recognized between human cherubism and our SH3BP2 cherubism mice. Although heterozygous SH3BP2 mutations are sufficient to cause autosomal dominant cherubism in humans, homozygous SH3BP2 mutations are required to cause facial swelling with jawbone destruction in mice.[3,4,7] In addition, homozygous SH3BP2 cherubism mice develop much more severe systemic inflammatory lesions outside the craniofacial skeleton that have not been reported in human cherubism patients.[3,7] In support of these facts, a recent study showed that the efficacy of imatinib, a BCR-ABL fusion protein inhibitor, differs between human and mouse cherubism, suggesting that the key signaling mechanisms that cause human cherubism are not identical to those in mice.[41,42] SYK has been shown to be a promising therapeutic target for cherubism in our studies with SH3BP2 cherubism mice.[3,43] Given the possible differences in cherubism pathogenesis between humans and mice, it may be conceivable that SYK inhibitor treatment for human cherubism may not be as effective as for cherubism in mice.

We also investigated the role of OGFRL1 in macrophages based on the hypothesis that OGFRL1 and SH3BP2 mutations share some of the pathogenic pathways resulting in cherubism. Since our previous studies showed that the SH3BP2 cherubism mutation increased macrophage inflammation and RANKL-induced osteoclastogenesis, *Ogfrl1*$^{-/-}$ BMMs were stimulated with LPS, TNF-α, or RANKL. However, we found no evidence that OGFRL1 controls macrophage inflammation and osteoclastogenesis. Consistent with these results, no significant DEGs were identified by RNA-seq analysis of *Ogfrl1*$^{-/-}$ macrophages or single-cell RNA-seq analysis of *Ogfrl1*$^{-/-}$ BM cells compared to these *Ogfrl1*$^{+/+}$ cells. These results suggest that the impact of OGFRL1 on macrophages and osteoclasts is not the same between human and mice. Further extensive investigations will be required to determine the function of OGFRL1 in human myeloid lineage cells compared to that in mouse myeloid lineage cells.

The mouse is the most commonly used model organism in human disease research.[44] In particular, knockout mouse models have been an invaluable resource for the study of rare diseases.[45,46] However, despite being such a well-established model, the suitability and validity of the mouse for recapitulating human disease have been controversial, for example, in studies comparing human and mouse immune functions and responses.[47-50] Notably, according to a report, null mutations in human and mouse orthologs often result in different phenotypes, and more than 20% of human essential genes have nonessential orthologs in mice.[51] Our investigation of OGFRL1 knockout and knock-in mice, which stemmed from the discovery of OGFRL1 loss-of-function mutations in cherubism families, supports the idea that studying human diseases using mouse models may not always lead to beneficial outcomes. Also, it suggests that OGFRL1 plays much more significant roles in humans than in mice. The discrepancies may be due to species-specific phenotypic thresholds, life spans, and living environments that involve different microbial conditions.

Despite our efforts to characterize *Ogfrl1*$^{-/-}$ and *Ogfrl1*$^{Del\text{-}c/Del\text{-}c}$ mice, the current study has limitations that should be addressed in future investigations. To conclude whether OGFRL1 loss-of-function mice recapitulate human cherubism and to determine the role of OGFRL1 *in vivo*, the use of other oral disease models[52] or different genetic backgrounds other than C57BL/6 will be essential. Also, we cannot exclude the possibility of compensation for OGFRL1 functions by other genes/proteins in mice. Genetically, the identification of additional cherubism patients carrying *OGFRL1* mutations and the study of induced pluripotent stem (iPS) cells from these affected individuals or iPS cells introduced with OGFRFL1 loss-of-function mutations will be important to complement the current study. Although highly unlikely, it is also conceivable that our findings in *OGFRL1* by WES are indeed coincidental and that other DNA variants in regulatory elements (eg, for *SH3BP2* transcription), introns, or non-coding RNA genes contribute to the development of cherubism in these families. To explore whether loss-of-function of OGFRL1 causes cherubism by upregulating SH3BP2 expression, investigation of SH3BP2 protein levels in patient tissue samples would be important.

In conclusion, we discovered OGFRL1 loss-of-function mutations in 2 unrelated autosomal recessive cherubism families with different ethnic backgrounds. However, OGFRL1 loss-of-function mice did not recapitulate the characteristic features of cherubism. Identification of additional cherubism patients with OGFRL1 mutations and clinical characterization of these patients will be necessary to determine the functions of OGFRL1 in humans. Our *Ogfrl1*$^{-/-}$ and *Ogfrl1*$^{Del\text{-}c/Del\text{-}c}$ mouse lines will serve as essential tools to complement such human cherubism studies.

Limitations in the current genetic study: We acknowledge the limitations of our genetic approach in the current cherubism study. Our strategy for identifying a second gene causing cherubism is based on the objective assumptions that exonic mutations in the same gene are causative for cherubism in both families and that genetic diseases in consanguineous families can be caused by autosomal recessive and homozygous gene mutations located in the identical-by-descent regions of the genome. Therefore, it is important to note that there is still a possibility that homozygous DNA variants in the *OGFRL1* gene region other than the *OGFRL1* exons or compound heterozygous or homozygous variants outside of the *OGFRL1* gene may be responsible for cherubism in the consanguineous families examined in this study. However, we believe that the probability is extremely low and that such scenarios are very unlikely to happen.

Acknowledgments

M.K. is a recipient of a fellowship from the Brain Circulation Program to Develop New Leaders for International Dental Education Course through international collaborative dental research, Japan, and of a fund for young researchers from the Japanese Society of Periodontology. T.Y. is a recipient of the Japan Society for the Promotion of Science (JSPS) Overseas Research Fellowship.

Author contributions

Mizuho Kittaka (Formal analysis, Investigation, Validation, Visualization, Writing—original draft, Writing—review & editing), Noriyoshi Mizuno (Conceptualization, Formal analysis, Investigation, Validation, Writing—review & editing), Hiroyuki Morino (Formal analysis, Investigation, Methodology, Validation, Writing—review & editing), Tetsuya Yoshimoto (Formal analysis, Investigation, Writing—review & editing), Tianli Zhu (Methodology, Writing—review & editing), Sheng Liu (Formal analysis, Writing—review & editing), Ziyi Wang (Formal analysis, Writing—review & editing), Kotoe Mayahara (Formal analysis, Investigation, Writing—review & editing), Kyohei Iio (Formal analysis, Investigation, Writing—review & editing), Kaori Kondo (Formal analysis, Investigation, Writing—review & editing), Toshio Kondo (Formal analysis, Investigation, Writing—review & editing), Tatsuhide Hayashi (Formal analysis, Investigation, Writing—review & editing), Sarah Coghlan (Formal analysis, Investigation, Writing—review & editing), Yayoi Teno (Formal analysis, Investigation, Writing—review & editing), Andrew Anh Phung Doan (Formal analysis, Investigation, Writing—review & editing), Marcus Levitan (Formal analysis, Investigation, Writing—review & editing), Roy B. Choi (Formal analysis, Investigation, Writing—review & editing), Shinji Matsuda (Formal analysis, Investigation, Writing—review & editing), Kazuhisa Ouhara (Formal analysis, Investigation, Writing—review & editing), Jun Wan (Formal analysis, Investigation, Writing—review & editing), Annelise M. Cassidy (Methodology, Resources, Writing—review & editing), Stephane Pelletier (Methodology, Resources, Writing—review & editing), Sheela Nampoothiri (Resources, Writing—review & editing), Andoni J. Urtizberea (Resources, Writing—review & editing), Alexander G. Robling (Formal analysis, Investigation, Writing—review & editing), Mitsuaki Ono (Formal analysis, Investigation, Writing—review & editing), Hideshi Kawakami (Formal analysis, Investigation, Resources, Writing—review & editing), Ernst J. Reichenberger (Conceptualization, Resources, Supervision, Writing—review & editing), and Yasuyoshi Ueki (Conceptualization, Formal analysis, Funding acquisition, Investigation, Resources, Supervision, Validation, Visualization, Writing—original draft, Writing—review & editing)

Supplementary material

Supplementary material is available at *JBMR Plus* online.

Funding

The research reported in this publication was supported by the National Institute of Dental and Craniofacial Research (R21DE030561, R01DE025870, R01DE025870-06S1, R01DE032036-01A1 to Y.U.).

Conflicts of interest

All authors state that they have no conflicts of interest.

Data availability

Human genetic data are available upon reasonable request and institutional approval. All animal data are available through the corresponding authors or GEO (GSE247887, GSE247888, and GSE247889).

References

1. Papadaki ME, Lietman SA, Levine MA, Olsen BR, Kaban LB, Reichenberger EJ. Cherubism: best clinical practice. *Orphanet J Rare Dis*. 2012;7(Suppl 1):S6. https://doi.org/10.1186/1750-1172-7-S1-S6
2. Reichenberger EJ, Levine MA, Olsen BR, Papadaki ME, Lietman SA. The role of SH3BP2 in the pathophysiology of cherubism. *Orphanet J Rare Dis*. 2012;7(Suppl 1):S5. https://doi.org/10.1186/1750-1172-7-S1-S5
3. Yoshitaka T, Mukai T, Kittaka M, et al. Enhanced TLR-MYD88 signaling stimulates autoinflammation in SH3BP2 cherubism mice and defines the etiology of cherubism. *Cell Rep*. 2014;8(6):1752–1766. https://doi.org/10.1016/j.celrep.2014.08.023
4. Prod'Homme V, Boyer L, Dubois N, et al. Cherubism allele heterozygosity amplifies microbe-induced inflammatory responses in murine macrophages. *J Clin Invest*. 2015;125(4):1396–1400. https://doi.org/10.1172/JCI71081
5. Ueki Y, Tiziani V, Santanna C, et al. Mutations in the gene encoding c-Abl-binding protein SH3BP2 cause cherubism. *Nat Genet*. 2001;28(2):125–126. https://doi.org/10.1038/88832
6. Levaot N, Voytyuk O, Dimitriou I, et al. Loss of Tankyrase-mediated destruction of 3BP2 is the underlying pathogenic mechanism of cherubism. *Cell*. 2011;147(6):1324–1339. https://doi.org/10.1016/j.cell.2011.10.045
7. Ueki Y, Lin CY, Senoo M, et al. Increased myeloid cell responses to M-CSF and RANKL cause bone loss and inflammation in SH3BP2 "cherubism" mice. *Cell*. 2007;128(1):71–83. https://doi.org/10.1016/j.cell.2006.10.047
8. Mukai T, Ishida S, Ishikawa R, et al. SH3BP2 cherubism mutation potentiates TNF-alpha-induced osteoclastogenesis via NFATc1 and TNF-alpha-mediated inflammatory bone loss. *J Bone Miner Res*. 2014;29(12):2618–2635. https://doi.org/10.1002/jbmr.2295
9. Mukai T, Gallant R, Ishida S, et al. SH3BP2 gain-of-function mutation exacerbates inflammation and bone loss in a murine collagen-induced arthritis model. *PLoS One*. 2014;9(8):e105518. https://doi.org/10.1371/journal.pone.0105518
10. Mukai T, Gallant R, Ishida S, et al. Loss of SH3 domain-binding protein 2 function suppresses bone destruction in tumor necrosis factor-driven and collagen-induced arthritis in mice. *Arthritis Rheumatol*. 2015;67(3):656–667. https://doi.org/10.1002/art.38975
11. Nagasu A, Mukai T, Iseki M, et al. Sh3bp2 gain-of-function mutation ameliorates lupus phenotypes in B6.MRL-Fas(lpr) mice. *Cells*. 2019;8(5):402. https://doi.org/10.3390/cells8050402
12. Kawahara K, Mukai T, Iseki M, et al. SH3BP2 deficiency ameliorates murine systemic lupus erythematosus. *Int J Mol Sci*. 2021;22(8):4169. https://doi.org/10.3390/ijms22084169
13. Kittaka M, Yoshimoto T, Schlosser C, et al. Microbe-dependent exacerbated alveolar bone destruction in heterozygous cherubism mice. *JBMR Plus*. 2020;4(6):e10352. https://doi.org/10.1002/jbm4.10352
14. Kittaka M, Yoshimoto T, Schlosser C, et al. Alveolar bone protection by targeting the SH3BP2-SYK axis in osteoclasts. *J Bone Miner Res*. 2020;35(2):382–395. https://doi.org/10.1002/jbmr.3882
15. Kittaka M, Yoshimoto T, Hoffman H, Levitan ME, Ueki Y. RANKL-independent osteoclastogenesis in the SH3BP2 cherubism mice. *Bone Rep*. 2020;12:100258. https://doi.org/10.1016/j.bonr.2020.100258
16. Morino H, Miyamoto R, Ohnishi S, Maruyama H, Kawakami H. Exome sequencing reveals a novel TTC19 mutation in an autosomal recessive spinocerebellar ataxia patient. *BMC Neurol*. 2014;14(1):5. https://doi.org/10.1186/1471-2377-14-5
17. Hagiwara K, Morino H, Shiihara J, et al. Homozygosity mapping on homozygosity haplotype analysis to detect recessive disease-causing genes from a small number of unrelated, outbred patients. *PLoS One*. 2011;6(9):e25059. https://doi.org/10.1371/journal.pone.0025059
18. Kittaka M, Yoshimoto T, Levitan ME, et al. Osteocyte RANKL drives bone resorption in mouse ligature-induced periodontitis. *J Bone Miner Res*. 2023;38(10):1521–1540. https://doi.org/10.1002/jbmr.4897
19. Yoshimoto T, Kittaka M, Doan AAP, et al. Osteocytes directly regulate osteolysis via MYD88 signaling in bacterial bone

infection. *Nat Commun*. 2022;13(1):6648. https://doi.org/10.1038/s41467-022-34352-z
20. Wang X, Kittaka M, He Y, Zhang Y, Ueki Y, Kihara D. OC_Finder: osteoclast segmentation, counting, and classification using watershed and deep learning. *Front Bioinform*. 2022;2:819570. https://doi.org/10.3389/fbinf.2022.819570
21. Aliprantis AO, Ueki Y, Sulyanto R, et al. NFATc1 in mice represses osteoprotegerin during osteoclastogenesis and dissociates systemic osteopenia from inflammation in cherubism. *J Clin Invest*. 2008;118(11):3775–3789. https://doi.org/10.1172/JCI35711
22. Machado RA, Pontes H, Pires FR, et al. Clinical and genetic analysis of patients with cherubism. *Oral Dis*. 2017;23(8):1109–1115. https://doi.org/10.1111/odi.12705
23. Guettler S, LaRose J, Petsalaki E, et al. Structural basis and sequence rules for substrate recognition by Tankyrase explain the basis for cherubism disease. *Cell*. 2011;147(6):1340–1354. https://doi.org/10.1016/j.cell.2011.10.046
24. Zagon IS, Verderame MF, McLaughlin PJ. The biology of the opioid growth factor receptor (OGFr). *Brain Res Brain Res Rev*. 2002;38(3):351–376. https://doi.org/10.1016/S0165-0173(01)00160-6
25. Zagon IS, Verderame MF, Zimmer WE, McLaughlin PJ. Molecular characterization and distribution of the opioid growth factor receptor (OGFr) in mouse. *Brain Res Mol Brain Res*. 2000;84(1-2):106–114. https://doi.org/10.1016/S0169-328X(00)00232-1
26. Zagon IS, Sassani JW, Kane ER, McLaughlin PJ. Homeostasis of ocular surface epithelium in the rat is regulated by opioid growth factor. *Brain Res*. 1997;759(1):92–102. https://doi.org/10.1016/S0006-8993(97)00238-2
27. Zagon IS, Sassani JW, McLaughlin PJ. Adaptation of homeostatic ocular surface epithelium to chronic treatment with the opioid antagonist naltrexone. *Cornea*. 2006;25(7):821–829. https://doi.org/10.1097/01.ico.0000224646.66472.aa
28. Zagon IS, Sassani JW, Verderame MF, McLaughlin PJ. Particle-mediated gene transfer of opioid growth factor receptor cDNA regulates cell proliferation of the corneal epithelium. *Cornea*. 2005;24(5):614–619. https://doi.org/10.1097/01.ico.0000153561.89902.57
29. Zagon IS, Donahue RN, Bonneau RH, McLaughlin PJ. B lymphocyte proliferation is suppressed by the opioid growth factor-opioid growth factor receptor axis: implication for the treatment of autoimmune diseases. *Immunobiology*. 2011;216(1-2):173–183. https://doi.org/10.1016/j.imbio.2010.06.001
30. Zagon IS, Donahue RN, Bonneau RH, McLaughlin PJ. T lymphocyte proliferation is suppressed by the opioid growth factor ([met(5)]-enkephalin)-opioid growth factor receptor axis: implication for the treatment of autoimmune diseases. *Immunobiology*. 2011;216(5):579–590. https://doi.org/10.1016/j.imbio.2010.09.014
31. Cheng F, McLaughlin PJ, Verderame MF, Zagon IS. The OGF-OGFr axis utilizes the p16INK4a and p21WAF1/CIP1 pathways to restrict normal cell proliferation. *Mol Biol Cell*. 2009;20(1):319–327. https://doi.org/10.1091/mbc.e08-07-0681
32. Seitz S, Barvencik F, Gebauer M, et al. Preproenkephalin (Penk) is expressed in differentiated osteoblasts, and its deletion in Hyp mice partially rescues their bone mineralization defect. *Calcif Tissue Int*. 2010;86(4):282–293. https://doi.org/10.1007/s00223-010-9344-5
33. Sogi C, Takeshita N, Jiang W, et al. Methionine enkephalin suppresses osteocyte apoptosis induced by compressive force through regulation of nuclear translocation of NFATc1. *JBMR Plus*. 2020;4(7):e10369. https://doi.org/10.1002/jbm4.10369
34. Thakur NA, DeBoyace SD, Margulies BS. Antagonism of the Met5-enkephalin-opioid growth factor receptor-signaling axis promotes MSC to differentiate into osteoblasts. *J Orthop Res*. 2016;34(7):1195–1205. https://doi.org/10.1002/jor.23135
35. Zagon IS, Donahue RN, McLaughlin PJ. Opioid growth factor-opioid growth factor receptor axis is a physiological determinant of cell proliferation in diverse human cancers. *Am J Physiol Regul Integr Comp Physiol*. 2009;297(4):R1154–R1161. https://doi.org/10.1152/ajpregu.00414.2009
36. Fanning J, Hossler CA, Kesterson JP, Donahue RN, McLaughlin PJ, Zagon IS. Expression of the opioid growth factor-opioid growth factor receptor axis in human ovarian cancer. *Gynecol Oncol*. 2012;124(2):319–324. https://doi.org/10.1016/j.ygyno.2011.10.024
37. Zagon IS, Porterfield NK, McLaughlin PJ. Opioid growth factor - opioid growth factor receptor axis inhibits proliferation of triple negative breast cancer. *Exp Biol Med*. 2013;238(6):589–599. https://doi.org/10.1177/1535370213489492
38. Donahue RN, McLaughlin PJ, Zagon IS. Cell proliferation of human ovarian cancer is regulated by the opioid growth factor-opioid growth factor receptor axis. *Am J Physiol Regul Integr Comp Physiol*. 2009;296(6):R1716–R1725. https://doi.org/10.1152/ajpregu.00075.2009
39. Kren NP, Zagon IS, McLaughlin PJ. Mutations in the opioid growth factor receptor in human cancers alter receptor function. *Int J Mol Med*. 2015;36(1):289–293. https://doi.org/10.3892/ijmm.2015.2221
40. Yanagawa T, Sumiyoshi H, Higashi K, et al. Identification of a novel bone marrow cell-derived accelerator of fibrotic liver regeneration through mobilization of hepatic progenitor cells in mice. *Stem Cells*. 2019;37(1):89–101. https://doi.org/10.1002/stem.2916
41. Mukai T, Akagi T, Hiramatsu Asano S, et al. Imatinib has minimal effects on inflammatory and osteopenic phenotypes in a murine cherubism model. *Oral Dis*. 2023;29(3):1089–1101. https://doi.org/10.1111/odi.14073
42. Ricalde P, Ahson I, Schaefer ST. A paradigm shift in the management of cherubism? A preliminary report using imatinib. *J Oral Maxillofac Surg*. 2019;77(6):1278.e1–1278.e7. https://doi.org/10.1016/j.joms.2019.02.021
43. Yoshimoto T, Hayashi T, Kondo T, Kittaka M, Reichenberger EJ, Ueki Y. Second-generation SYK inhibitor entospletinib ameliorates fully established inflammation and bone destruction in the cherubism mouse model. *J Bone Miner Res*. 2018;33(8):1513–1519. https://doi.org/10.1002/jbmr.3449
44. Rosenthal N, Brown S. The mouse ascending: perspectives for human-disease models. *Nat Cell Biol*. 2007;9(9):993–999. https://doi.org/10.1038/ncb437
45. da Silva-Buttkus P, Spielmann N, Klein-Rodewald T, et al. Knockout mouse models as a resource for the study of rare diseases. *Mamm Genome*. 2023;34(2):244–261. https://doi.org/10.1007/s00335-023-09986-z
46. Cacheiro P, Haendel MA, Smedley D, International Mouse Phenotyping C, the Monarch I. New models for human disease from the International Mouse Phenotyping Consortium. *Mamm Genome*. 2019;30(5-6):143–150. https://doi.org/10.1007/s00335-019-09804-5
47. Seok J, Warren HS, Cuenca AG, et al. Genomic responses in mouse models poorly mimic human inflammatory diseases. *Proc Natl Acad Sci U S A*. 2013;110(9):3507–3512
48. Mestas J, Hughes CC. Of mice and not men: differences between mouse and human immunology. *J Immunol*. 2004;172(5):2731–2738. https://doi.org/10.4049/jimmunol.172.5.2731
49. Shay T, Jojic V, Zuk O, et al. Conservation and divergence in the transcriptional programs of the human and mouse immune systems. *Proc Natl Acad Sci U S A*. 2013;110(8):2946–2951. https://doi.org/10.1073/pnas.1222738110
50. Takao K, Miyakawa T. Genomic responses in mouse models greatly mimic human inflammatory diseases. *Proc Natl Acad Sci U S A*. 2015;112(4):1167–1172. https://doi.org/10.1073/pnas.1401965111

51. Liao BY, Zhang J. Null mutations in human and mouse orthologs frequently result in different phenotypes. *Proc Natl Acad Sci U S A*. 2008;105(19):6987–6992. https://doi.org/10.1073/pnas.0800387105

52. Fujii Y, Monteiro N, Sah SK, et al. Tlr2/4-mediated hyperinflammation promotes cherubism-like jawbone expansion in Sh3bp2 (P416R) knockin mice. *JBMR Plus*. 2022;6(1):e10562. https://doi.org/10.1002/jbm4.10562